Warming-to-Cooling Reversal of Overflow-Derived Water Masses in the Irminger Sea During 2002–2021

Damien Desbruyères, Eva Prieto Bravo, Virginie Thierry, Herlé Mercier, Pascale Lherminier, Cécile Cabanes, Tiago Biló, Nora Fried, M. Femke de Jong

1 # Warming-to-cooling reversal of overflow-derived water masses in the Irminger Sea
2 # during 2002-2021.

3

4 Damien G. Desbruyères[1], Eva Prieto Bravo[1], Virginie Thierry[1], Herlé Mercier[1], Pascale Lherminier[1], Cécile
5 Cabanes[1], Tiago C. Biló[2], Nora Fried[3], M. Femke De Jong[3].

6
7 [1]University of Brest, CNRS, Ifremer, IRD, Laboratoire d'Océanographie Physique et Spatiale (UMR 6523 LOPS), Plouzané, France
8
9 [2]Scripps Institution of Oceanography, University of Califonia San Diego.
10
11 [3]Department of Ocean Systems, NIOZ, Royal Netherlands Institute for Sea Research, Texel, The Netherlands
12

13 Corresponding author: Damien Desbruyères (damien.desbruyeres@ifremer.fr)

14

15 ## Key Points:

16 - Shipboard, Deep-Argo, and mooring data capture a warming-to-cooling reversal of Lower North
17   Atlantic Deep Water in the Irminger Sea in 2014.
18
19 - The cooling trend is statistically-significant and has likely accelerating in recent years, reaching -16
20   ± 6 m°C yr^{-1} during $2016 - 2021$
21
22 - Denmark Strait Overflow Water has warmed and cooled significantly faster than Iceland Scotland
23   Overflow Water during $2002 - 2021$.

24
25

26   Abstract

27   Shipboard hydrography along the A25-Ovide section (2002 – 2018) is combined with a high-resolution
28   mooring array (2014 – 2020) and a regional fleet of Deep-Argo floats (2016 – 2021) to describe temperature
29   changes of overflow-derived water masses in the Irminger Sea. Removing dynamical influences enables to
30   identify a new statistically-significant trend reversal in Iceland Scotland Overflow Water (ISOW) and
31   Denmark Strait Overflow Water (DSOW) core temperatures in the mid-2010s. A basin-wide cooling trend
32   of -16 ± 6 m°C yr^{-1} during 2016 – 2021 – but reaching as strong as -44 ± 13 m°C yr^{-1} for DSOW in recent
33   years – is found to interrupt a warming phase that was prevailing since the late 1990's. The absence of an
34   apparent reversal in the Nordic Seas and the faster changes detected in DSOW compared to ISOW point
35   out the entrainment of subpolar signals within the overflows near the Greenland-Iceland-Scotland sills as
36   a most likely driver.

37   Plain Language Summary

38   The North Atlantic Deep Water is one of the most voluminous water masses of the global ocean. Its deepest
39   constituent – the Lower North Atlantic Deep Water (LNADW) – forms in the Nordic Seas before cascading
40   into the North Atlantic at the Greenland-Iceland-Scotland sills and progressing south towards the Southern
41   Ocean. The temperature and salinity of LNADW are known to obey decadal trends in response to forcing in
42   its source regions as well as subsequent mixing with surrounding and overlying water masses during its
43   Atlantic journey. Here, repeated measurements from oceanographic vessels, continuous monitoring with
44   moored instrumentations, and autonomous Deep-Argo floats in the Irminger Sea (east of Greenland) during
45   2002 – 2021 are used to reveal a new warming-to-cooling reversal of LNADW in 2014. This signal, which
46   presumably originates in the entrainment of upper and intermediate ocean variability near the Greenland-
47   Iceland-Scotland sills, will progressively travel southward within the lower branch of the Atlantic Meridional
48   Overturning Circulation.

49   1.   Introduction

50   The warming of the global ocean remains an unabated consequence of human-driven climate change (IPCC
51   et al., 2021). The progressive rise in atmospheric greenhouse gas concentrations causes an extra downward
52   heat flux of about 0.6-0.8 W m^{-2} through the sea surface (Desbruyères et al., 2017; Johnson et al., 2016),
53   with a likely acceleration in recent years (Von Schuckmann et al., 2020) and several ramifications on sea-
54   level rise (Tebaldi et al., 2021), ocean stratification and mixing processes (Sallée et al., 2021), or ocean
55   deoxygenation and carbon sequestration (Keeling et al., 2009). This global warming rate is often inferred
56   from *in situ* observations of ocean heat content, which became well constrained in the mid-2000's owing
57   to the completed implementation of the global network of 0 – 2000 m Argo profiling platforms (Riser et al.,
58   2016). A significant source of uncertainty on global and regional OHC increase remains however linked to
59   the comparatively poor systematic and homogeneous sampling of the deep ocean below 2000 (Garry et
60   al., 2019; Purkey & Johnson, 2010). This issue contributed to motivate the deep extension of the Argo array
61   since the mid 2010's, the Deep-Argo program (Johnson et al., 2015; Roemmich et al., 2019).
62
63   Key regions for deep ocean heat storage variability were targeted to conduct Deep-Argo pilot experiments.
64   One of them is the Subpolar North Atlantic Ocean (SPNA) where a cold and dense water mass – the North
65   Atlantic Deep Water (NADW) – constantly propagates interannual to multi-decadal thermohaline and
66   biogeochemical signals over large spatial scales (Talley et al., 2011). The climatic significance of NADW is
67   also witnessed by the on going deployment of a Canada – Greenland – Scotland mooring array (the
68   Overturning in the Subpolar North Atlantic Program; OSNAP), which enables since 2014 a continuous
69   monitoring of its thermohaline properties and volume transport (Lozier et al., 2019). However, while much
70   is known about the intrinsic variability of upper NADW (UNADW) formed in the SPNA through deep

71 convective mixing and efficiently monitored with core Argo floats above 2000 m (Yashayaev & Loder, 2016),
72 local thermohaline changes within the lower NADW (LNADW) that originates in the Nordic Seas has
73 received less attention in the recent literature.
74
75 The LNADW is convectively formed in the Greenland and Norwegian Seas and enters the subpolar North
76 Atlantic via narrow cascading flows constrained by the shallow ridge (<1000 m) that extends from Scotland
77 to Greenland (Hansen & Østerhus, 2000). As it overflows, LNADW entrains surrounding and mixes with,
78 less dense, Atlantic waters to form overflow-derived water masses, namely the Iceland-Scotland Overflow
79 Water (ISOW) and the Denmark Strait Overflow Water (DSOW). Dickson et al. (2002) reported on a long-
80 term (1965-2002) gradual freshening of both overflow-derived water masses in the Irminger and Labrador
81 seas. This was partly attributed to an upstream freshening of the source waters in the Nordic Seas, and
82 partly to mixing with upper and intermediate water masses southeast of Iceland and in the Irminger Seas
83 that were themselves freshening at equal or greater rates. A reversal of this trend in the late 1990's was
84 subsequently observed, with ISOW and DSOW entering a warming and salinification phase until the year
85 2006 at least (van Aken & de Jong, 2012; Holliday et al., 2008; Sarafanov et al., 2007, 2010). Here, we pursue
86 those efforts and analyze the recent variability in ISOW and DSOW properties in the Irminger Sea using 9
87 biennial occupations (2002 − 2018) of the Portugal-Greenland A25-Ovide section (Daniault et al., 2016;
88 Mercier et al., 2015), the 2017 occupation of the Reykjanes Ridge Experiment (RREX) sections (Petit et al.,
89 2018), 6 years of OSNAP mooring data (2014 - 2020), and about 6 years (2016 − 2021) of continuous Deep-
90 Argo observations. We report LNADW temperature changes in the Irminger Sea and discuss their likely
91 drivers, distinguishing local dynamics and remote advection from intrinsic ISOW and DSOW anomalies. We
92 also further demonstrate the high scientific value of sustained a Deep-Argo array (Foppert et al., 2021;
93 Johnson, 2019; Johnson et al., 2020; Kobayashi, 2018; Racapé et al., 2019; Zilberman et al., 2020), and to
94 particularly highlight its usefulness alongside repeat shipboard hydrography and moored instrumentations
95 for a comprehensive monitoring of deep temperature changes. The datasets and the methodology are
96 described in Section 2. Results are provided in Section 3 and summarized and discussed in Section 4.

2. Materials and Methods

### 2.1. Repeat hydrography, Deep-Argo, and OSNAP datasets

99 The geographical distribution of all profiles (i.e. shipboard and floats) and the location of moorings is shown
100 in Figure 1. Nine years of hydrographic data were provided by biennial (summer) repetitions of the
101 Greenland–Portugal A25-Ovide line from 2002 to 2018 (Daniault et al., 2016). Gridded fields of
102 temperature and salinity (1 db x 7 km) were interpolated linearly on an annual grid to derive 2005-2017
103 climatological fields and allow consistent comparisons with the concomitant World Ocean Atlas 2018
104 climatology (see below). Additional shipboard hydrography profiles gathered along the eastern flank of the
105 Reykjanes Ridge in 2017 were also used (Petit et al., 2018), as well as 484 full-depth temperature and
106 salinity profiles provided by 8 Deep-Argo floats deployed in the Irminger Basin through 2016-2021. Those
107 were quality-controlled and salinity was adjusted to reference profiles following the procedure specified
108 for Deep-Argo floats (Wong et al, 2021).
109
110 The OSNAP datasets consist of two mooring arrays covering the western flank of the Reykjanes Ridge
111 (OSNAP-EI hereafter) and the Irminger Sea's western boundary (OSNAP-WI hereafter). All moorings
112 measured hydrographic properties every 15 minutes to one hour between July-August 2014 and July 2020.
113 Below 1000 m, these instruments are vertically separated by a few hundreds of meters. In the present
114 study, moored calibrated temperature and salinity data were low-pass filtered using a 41-hr sixth-order
115 Butterworth filter and subsampled to daily resolution. Hydrographic fields were then vertically

116   (horizontally) interpolated onto regular grids using a piecewise Hermite cubic polynomial (linear)
117   interpolation schemes. Additional information on OSNAP data calibration procedures, processing, and
118   interpolation are already published (Le Bras et al., 2018; Fried & de Jong, 2022; Johns et al., 2021; de Jong
119   et al., 2020).
120
121   2.2. WOA18 and OV18 climatologies
122
123   The 2005 – 2017 climatology of θ in the Irminger Basin (30°- 44°W, 54°- 66°N) was extracted from the 1/4°
124   global World Ocean Atlas 2018 (WOA18).

125   Using this most recent decade as a
126   climatological baseline should minimize the
127   risk of aliasing spatial and temporal variability
128   due to sparse and non-regular data
129   distribution. To further evaluate this risk, we
130   follow Kobayashi (2018) and construct an
131   independent regional climatology from the
132   well-constrained 2005-2017 mean A25-Ovide
133   θ field. This construction assumes along-
134   isopycnal potential vorticity (*f/H*) conservation
135   as water masses flow cyclonically in the
136   Irminger Sea (where *f* is the Coriolis parameter
137   and *H* the ocean depth, here obtained from a
138   smoothed version of the 2′ ETOPO
139   topography). North of A25-Ovide, the
140   climatological temperature along a given *f/H*
141   contours was estimated as:
142
143
144
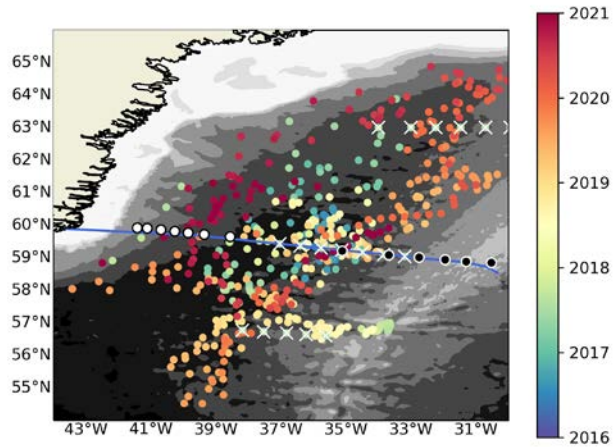
Figure 1. *Study domain along with the A25-Ovide section (blue line), RREX 2017 (white crosses), WI and EI OSNAP mooring locations (white and black circles, respectively), and Deep Argo floats profiles with dots colored by their decimal year. Background shading are 500m-spaced isobaths.*

$$\langle\theta_{f/H}\rangle = (1-l)*\langle\theta_W{}^{A25}\rangle + l*\langle\theta_E{}^{A25}\rangle \qquad \text{equation 1}$$

147   where $\langle\theta_W{}^{A25}\rangle$ and $\langle\theta_E{}^{A25}\rangle$ are the climatological temperature at the western and eastern intersections
148   of the *f/H* contour with the section, and l is a weight calculated from the along-contour distance between
149   the western intersection and the point on the *f/H* contour where the estimation is to be made (divided by
150   the total length of the contour). South of A25-Ovide, the climatological temperature along a given *f/H*
151   contours was set from the closest intersection of this *f/H* contour with the section. We will refer to this
152   A25-Ovide climatological product as OV18 hereafter.
153
154   2.3. Heave and spice
155
156   An isopycnal decomposition of θ anomalies into θ_{HEAVE} (anomalies at a fixed pressure associated with
157   isopycnal displacements) and θ_{SPICE} (anomalies on potential density surfaces) is carried out (Bindoff &
158   McDougall, 1994) . Temperature and pressure profiles were interpolated onto a 0.001-resolution σ_2 vertical
159   grid. Temperature anomalies on fixed σ_2 surfaces yield the θ_{SPICE} component in σ_2 space, while pressure
160   anomalies at fixed σ_2 surfaces multiplied by the local vertical background temperature gradient yield the
161   θ_{HEAVE} component in σ_2 space. Both components are eventually re-gridded on a uniform grid at 10-dbar

162   intervals using the pressure of σ_2 surfaces, and the departure of their sum from the true anomalies or
163   trends provide the error of the decomposition. This method has been regularly applied in water mass
164   analyses in the North Atlantic as an indicative means to infer the sources or mechanisms of the observed
165   changes (e.g. Häkkinen et al., 2015b). Here, we will interpret θ_{SPICE} as the advection of a remote
166   thermohaline signals within ISOW and DSOW (e.g. due to anomalous air-sea heat exchanges in the Nordic
167   Seas, or to the entrainment of anomalies from overlying layers near the sills). On the other hand,
168   θ_{HEAVE} will be interpreted as remote changes in ISOW and/or DSOW formation rates or local dynamical
169   changes (e.g. wind-driven lateral shift of geostrophic currents). We will primarily focus on θ_{SPICE}, and
170   consider θ_{HEAVE} as the dynamical signal to be removed to reveal intrinsic water mass property changes.
171
172   2.4. Linear trends and uncertainties from float data
173
174   We compute linear θ trends and associated uncertainties from Deep-Argo observations following Johnson
175   et al. (2019). Trends are computed at each pressure levels from all profiles regardless of their location, with
176   standard errors and 95% confidence intervals derived from the residuals to the linear fit using standard
177   methodology for unweighted least-square regressions. To do so, we obtain the number of degrees of
178   freedom at each pressure level by assuming that all floats are statistically independent of each other (i.e.
179   that their horizontal separation length scales are greater than that of the dominant transient features in
180   the region, typically eddies). However, time series from individual float are serially correlated, and a typical
181   decorrelation length scale of 60 days computed globally from Argo data at 1800 db is used (Johnson et al.,
182   2015), and assumed to prevail at greater depth due to the vertically-uniform banded structure of θ trends
183   observed in the region (Desbruyères et al., 2014).

184   ## 3. Results

185   3.1. The climatological picture
186
187   The deep stratification is dominated by θ, with an east-west asymmetry associated with the northward
188   advection of relatively warm waters at mid-depth along the western flank of Reykjanes Ridge and the
189   southward advection of relatively cold waters along the deepest portion of Greenland continental slope
190   (Figure 2a). The presence of baroclinic boundary currents is revealed by the inshore plunging of isopycnal
191   surfaces above 2000 m on both side of the basin. The salinity section depicts the predominant salty
192   signature of ISOW spreading offshore from Reykjanes Ridge, and the fresh signatures of LSW above 1500
193   m in the interior and of DSOW above the western continental slope (Figure 2b). In the following, only the
194   water masses denser than σ_2 = 36.94 ($\sim\sigma_0$ = 27.80) will be considered in order to willingly exclude LSW
195   signals and focus the analysis of changes on LNADW, which will be decomposed into ISOW and DSOW using
196   σ_2 = 37.07 ($\sim\sigma_0$ = 27.88) (Daniault et al., 2016).
197
198   The WOA18 and OV18 climatological fields of θ vertically-averaged within LNADW are shown in Figure 2b
199   and 2c, respectively. They both capture a broad warm-to-cold transition of the boundary current, which is
200   broader and patchier in WOA18 owing to the relatively coarse horizontal length scales used in the
201   interpolation scheme as well as the underlying uneven data distribution. OV18 shows a thinner and
202   gradually cooling boundary current as expected from the simple linear model (equation 1). A second,
203   maybe more striking, difference is a colder western basin interior in WOA18 than in OV18, which reflects
204   the lacking signature of DSOW inflow from Denmark Strait in the OV18 reconstruction (not shown). WOA18
205   and OV18 have been used side-by-side in Section 3c to estimate temperature anomalies from Deep-Argo
206   profiles. Their discrepancies were most exclusively reflected in θ_{HEAVE} due to the dependence of this
207   component to the background stratification (equation 2a). Because results were on the other hand

208   markedly similar for θ_{SPICE} – our focus herein – OV18-based diagnostics will be provided as supplementary
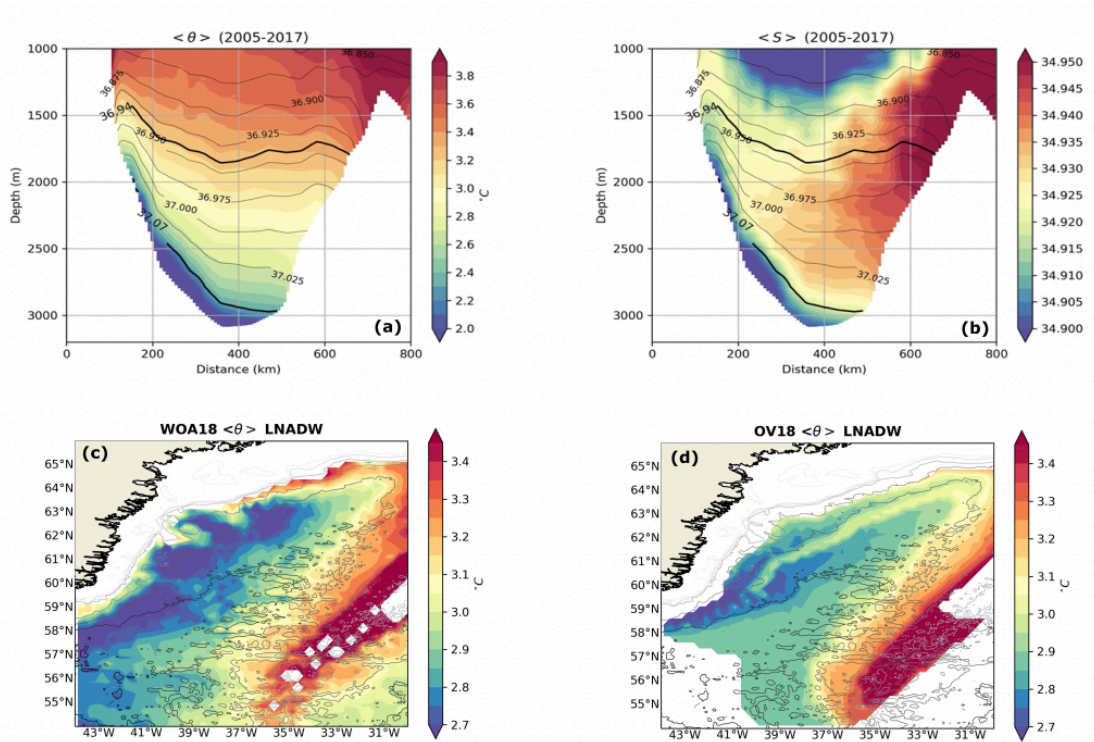209   materials.
210

Figure 2. *Climatological mean (2005-2017) of (a) conservative temperature and (b) salinity at the A25-Ovide section. Thin black lines show isopycnal σ_2 surfaces and thick black lines show σ_2 = 36.94 and σ_2 = 37.07 that are respectively used as an upper bound for LNADW and as a lower (upper) bound for ISOW (DSOW). (c) The 2005 – 2017 WOA18 field of conservative temperature averaged within the LNADW layer (i.e. below σ_2 = 36.94). (d) same as (c) but from OV18.*

211
212   3.2. Long-term changes measured at the A25-Ovide section
213
214   The 2002 – 2018 A25-Ovide dataset provides a local yet a long-term time series of LNADW θ anomalies in
215   the Irminger Sea. It shows a period of anomalously cold conditions (2002 – 2006) and a period of
216   anomalously warm condition (2014 – 2018) separated by a period of weak changes (2006 – 2014) (Figures
217   3a and 3b). The horizontally-averaged trend during 2002 – 2018 shows statistically-significant warming over
218   most of the LNADW vertical extent with a gradual decrease in magnitude from a maximum of 20 m°C yr^{-1}
219   at 1500 m to near zero at 3000 m, and a depth-averaged value of 10 ± 4 m°C yr^{-1} (black line in Figure 3c).
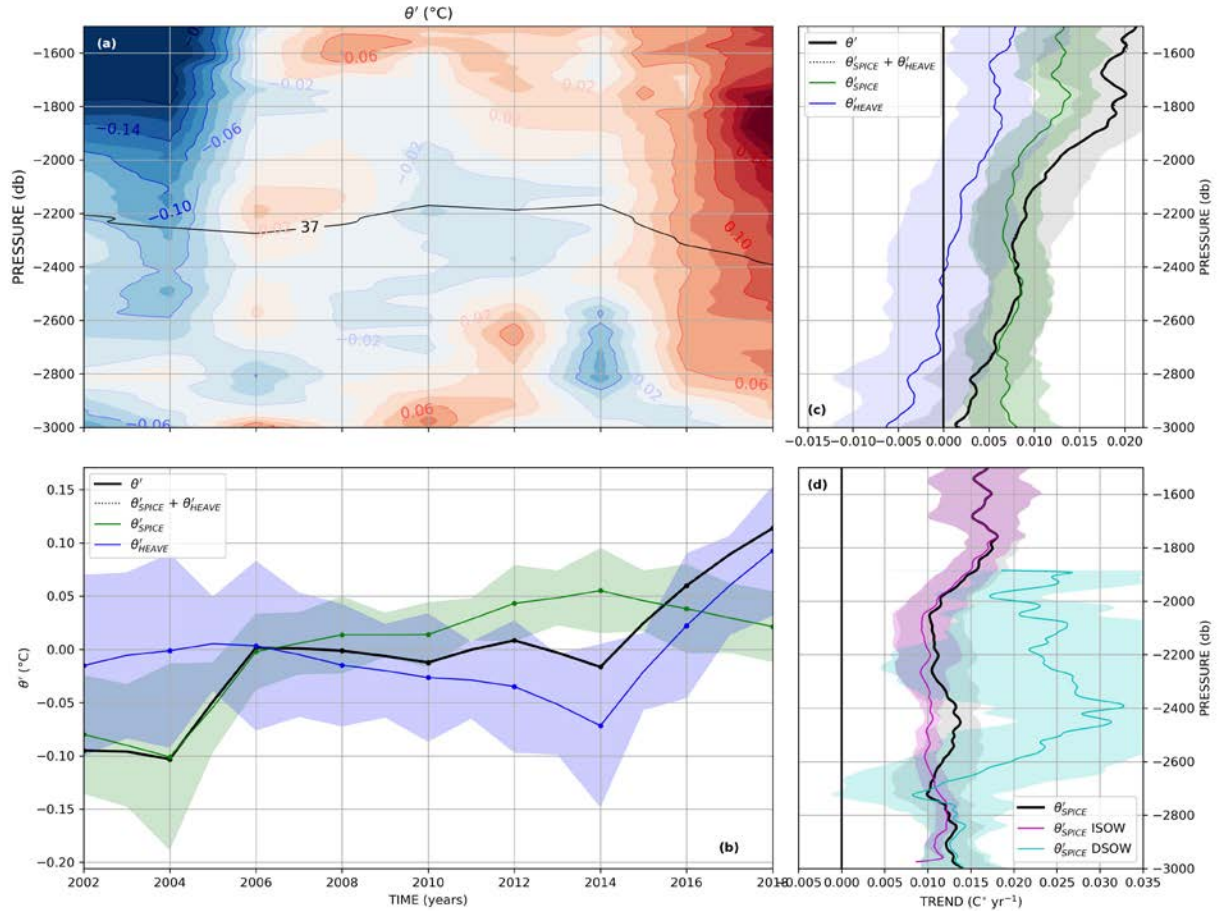
Figure 3. A25-Ovide analysis (2002 – 2018). *(a). Horizontally-averaged temperature anomalies within the LNADW layer (relative to the 2005-2017 period) at the A25-Ovide section. The black line shows σ_2 = 37 kg m^{-3}. (b) Temperature anomalies averaged within the LNADW layer (black) and decomposed into θ_{SPICE} and θ_{HEAVE} (green and blue, respectively). Their sum is shown with the dotted line and their respective spatial standard deviations are shaded. (c) The 2002 – 2018 linear temperature trends as a function of pressure averaged within the LNADW layer for each component (°C yr^{-1}). (d) The 2002 – 2014 linear θ_{SPICE} trends as a function of pressure averaged within the whole LNADW layer (black), within the ISOW layer (magenta), and within the DSOW layer (cyan). In both (c) and (d) shadings indicate 5-95% confidence limits.*

220 Decomposing θ anomalies into θ_{SPICE} and θ_{HEAVE} provides the fraction of the observed changes driven
221 by actual water mass property changes. θ_{SPICE} anomalies increased sharply between 2004 and 2006 before
222 gradually increasing at a slower rate until 2014 when cooling conditions appeared (green line in Figure 3b).
223 The horizontally-averaged θ_{SPICE} trend is positive and statistically-significant at all depths, with a depth-
224 averaged value of 8 ± 3 m°C yr^{-1} (green line in Figure 3c). On the other hand, θ_{HEAVE} is characterized by a
225 gradual cooling between 2006 and 2014 and a sharp warming afterwards (blue line in Figure 3b). This can
226 be also visualized with the changing depth of $\sigma_2 = 37$ – an isopycnal surface falling within the core of LNADW
227 (black line in Figure 3a). The depth-averaged θ_{HEAVE} trend is relatively weak (2 ± 5 m°C yr^{-1}) due to a
228 compensation between warming within the 1500 – 2400 m layer and cooling below, which is seemingly in
229 line with an adiabatic redistribution of water masses (blue line in Figure 3c). Statistical significance is not
230 reached except near 1800 m. Overall, LNADW in the Irminger Sea appear to have significantly warmed
231 during 2002 – 2018 at all depth levels, while local and/or remote dynamical changes enhanced and reduced

232 warming rates at constant pressure above and below 2400 m, respectively. Trends reversed in 2014
233 however, with a sharp downward displacement of isopycnal surfaces (supposedly driven by lateral shift of
234 geostrophic fronts at the boundaries – not shown) masking a return to a density-compensated cooling
235 phase for LNADW. This is further described below with the Deep-Argo and OSNAP datasets.
236
237   3.3. Recent changes measured by Deep-Argo floats and the OSNAP mooring array
238
239 Recurrent θ and S measurements in the Irminger Sea by Deep-Argo floats RREX hydrography surveys
240 provide key basin-scale information in recent years. During 2016-2021, most of the LNADW layer in the
241 Irminger Sea was significantly warmer than during 2005-2017, although cold LNADW anomalies are
242 sporadically found along the boundaries of the basin (Figure 4a). The 2016-2021 linear trend and its 95%
243 confidence interval at each pressure level within the LNADW layer is shown in Figure 4c (black line). Its
244 depth-averaged magnitude of -17 $\pm$ 19 m°C yr^{-1} hides a complicated vertical structure with statistical
245 significance restricted to those small portions of the water column where the trend magnitude is peaking
246 (e.g. 1600 m, 2100 m, and 2800 m). Again, the isopycnal decomposition reveals a key role for θ_{HEAVE} in
247 dictating this vertical structure, with peaking intensity potentially reflecting local volume changes of ISOW
248 and DSOW (blue line in Figure 4c). Most importantly, the trend in θ_{SPICE} is uniformly negative and
249 statistically-significant, with a depth-averaged trend of -16 $\pm$ 6 m°C yr^{-1} and bottom-intensified cooling rates
250 up to 60 m°C yr^{-1}(green line in Figure 4c). This shows the persistence of the warming-to-cooling reversal in
251 LNADW core temperature detected along A25-Ovide since 2014 (Figure 3b).
252
253 The horizontal pattern of θ_{SPICE} anomalies derived from Deep-Argo profiles is moreover illuminating
254 (Figure 4b). It shows a clear contrast between positive anomalies covering a broad area of the basin interior,
255 weakly positive and negative anomalies along the flank of Reykjanes Ridge, and strongly negative anomalies
256 off Greenland. This indicates that the 2014-2021 cooling trend of LNADW firstly appeared along the
257 boundary of the basin before progressively spreading into the interior, in line with the remote advection of
258 colder LNADW classes by the mean boundary-focused circulation. It also suggests a most significant
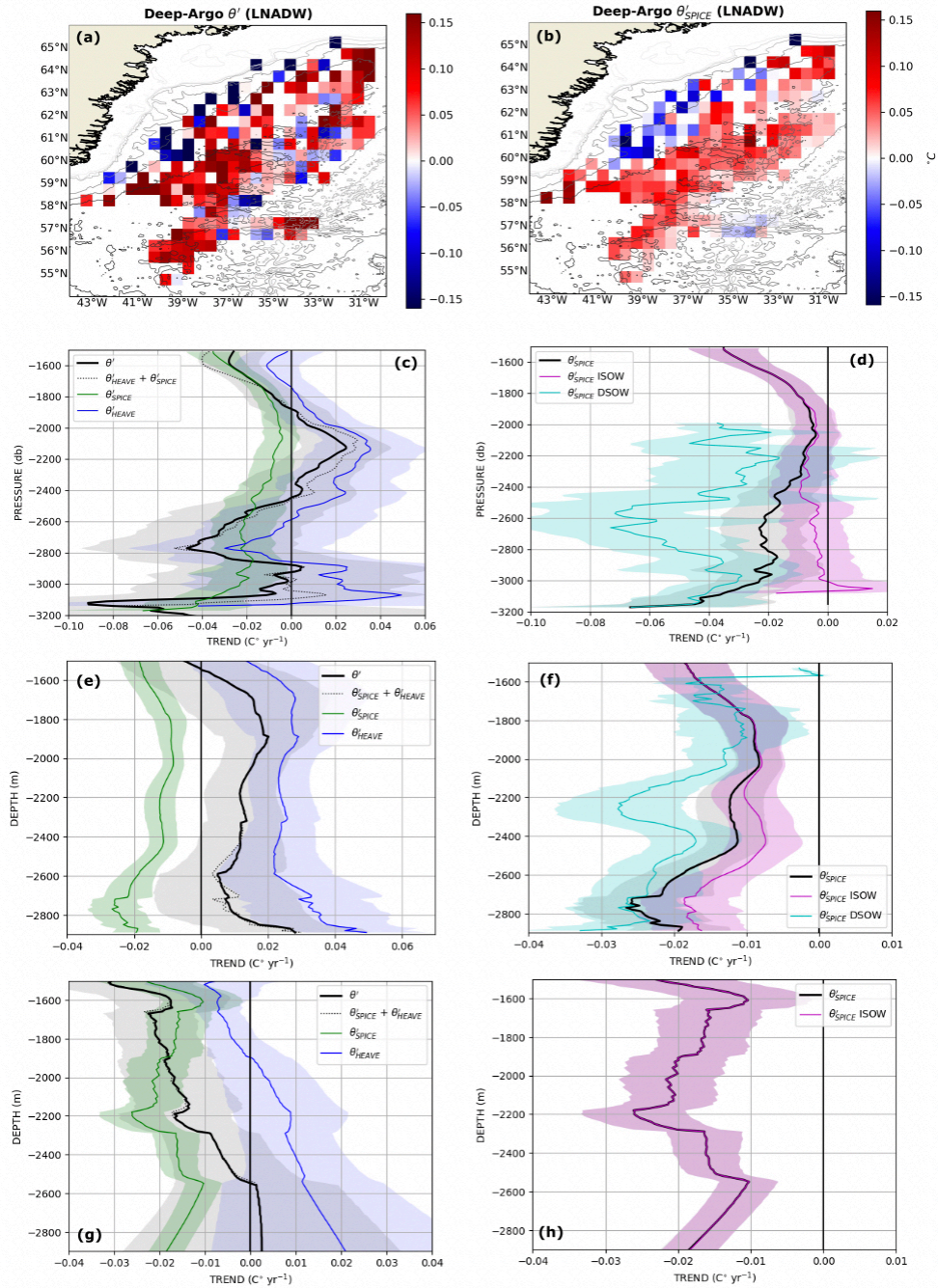259 decrease of DSOW temperature in recent years, as discussed in Section 3.4.
260
261

Figure 4. Deep-Argo (2016 − 2021) and OSNAP analysis (2014 − 2020). *(a) The 2016-2021 Deep Argo-based temperature anomalies relative to the 2005-2017 WOA18 climatology and averaged within the LNADW layer (i.e. below σ_2 = 36.94). Profiles were gridded at ¼° resolution for clarity. (b) Same as (a) but for θ_{SPICE}. (c) The linear temperature trends during 2016 − 2021 as a function of pressure averaged within the whole LNADW layer (black) decomposed into θ_{SPICE} and θ_{HEAVE} (green and blue, respectively, with their sum shown with the dotted line). (d) The 2016-2021 linear θ_{SPICE} trend as a function of pressure averaged within the whole LNADW layer (black), within the ISOW layer (magenta), and within the DSOW layer (cyan). (e, f) and (g, h) Same as (c, d) but from the OSNAP-WI and OSNAP-EI datasets, respectively. Shadings indicate 5-95% confidence limits.*

262

263   Finally, OSNAP-WI and OSNAP-EI provide local but high-resolution boundary-focused measurements during
264   2014 − 2020 and therefore a third independent estimate of LNADW variability. Applying the isopycnal
265   decomposition to gridded θ and S fields confirms the statistically-significant cooling of LNADW at both the
266   western and eastern side of the basin (Figure 4e and 4g, respectively), as well as the tendency for isopycnal
267   heave to oppose and mask this intrinsic trend in water mass property. The magnitude of mooring-based
268   θ_{HEAVE} trends can be expectedly relatively large (e.g. 25 ± 9 m°C yr^{-1} fro OSNAP-WI), since moorings
269   predominantly sample the highly dynamical boundary region where lateral geostrophic shifts and
270   temperature gradients (and hence isopycnal heave) are most significant. Most importantly, the magnitudes
271   of θ_{SPICE} trends are quantitatively in line with those captured by Deep-Argo during 2016 − 2021,
272   respectively reaching -12 ± 3 m°C yr^{-1} and -16 ± 5 m°C yr^{-1} across the OSNAP-WI and OSNAP-EI.

273

274   3.4. ISOW and DSOW contributions

275

276   We eventually quantify the respective signature of ISOW and DSOW on the observed LNADW θ_{SPICE} trends
277   and, in particular, on the Ovide-based warming phase (Figure 3d), and on the Deep-Argo-based, OSNAP-
278   WI-based and OSNAP-EI-based cooling phases (Figure 4d, 4f and 4h, respectively). During 2002 − 2014,
279   ISOW warmed at a depth-averaged rate of 12 ± 2 m°C yr^{-1}, before cooling at a rate of -11 ± 6 m°C yr^{-1} during
280   2016 − 2021 (Deep-Argo). Consistently, ISOW cooling rates measured at OSNAP-WI and OSNAP-EI during
281   2014 − 2020 were -10 ± 3 m°C yr^{-1} and -16 ± 5 m°C yr^{-1}, respectively. The magnitudes of DSOW θ_{SPICE}
282   trends were significantly larger, with a warming rate of 18 ± 8 m°C yr^{-1} during 2002 − 2014 and cooling rates
283   of -22 ± 6 m°C yr^{-1} during 2014 − 2020 at OSNAP-WI and of up to -44 ± 13 m°C yr^{-1} during 2016 − 2021 basin
284   wide. This apparent acceleration of the cooling trend is confirmed by computing the linear trend at OSNAP-
285   WI during 2017 − 2020 (i.e. close to the Deep-Argo time-span). The latter yields a rate of -38 ± 9 m°C yr^{-1},
286   in good agreement with the independent Deep-Argo-based estimate.

287

288

289   **4. Conclusion and discussion**

290

291   The deep layer of the Irminger Sea (∼1500 − 3000 m) underwent positive and negative temperature trends
292   over the last two decades (2002 − 2021) that were one order of magnitude larger than global and basin-
293   scale estimates within the same layer (Desbruyères et al., 2016). After removing heave-induced signals,
294   which most likely reflect wind-driven and/or buoyancy-driven geostrophic adjustments of boundary
295   currents and possibly water mass volume changes, we report from three independent datasets (shipboard
296   hydrography, Deep-Argo floats, and OSNAP moorings) a statistically-significant warming-to-cooling reversal
297   in the core temperature of overflow-derived water masses in the mid-2010's. The LNADW warmed during
298   2002 − 2014 at an average rate of 13 ± 3 m°C yr^{-1} and is cooling since then, with a suggested accelerating
299   rate of change reaching -16 ± 6 m°C yr^{-1} during 2016 - 2021. While those trends were consistently detected
300   within the two components of LNADW, their magnitudes were significantly larger for DSOW than for ISOW,
301   with their ongoing cooling notably reaching average rates of -44 ± 13 m°C yr^{-1} and -11 ± 6 m°C yr^{-1},
302   respectively.

303

304   Investigating the causes of the observed changes is beyond the scope of this descriptive study but the
305   patterns we report and the relevant literature can already enable a tentative explanation. While the gradual
306   warming of ISOW and DSOW in the Irminger Sea during 2002 − 2014 is not inconsistent with the reported
307   steady warming of the Nordic Seas, there has not been clear signs of sustained cooling in recent years in
308   this source region (Broomé et al., 2020). This suggests that the 2014 warming-to-cooling reversal of ISOW

309 and DSOW was most likely driven by the entrainment of SPNA signals within the overflow plumes at the
310 Greenland-Iceland-Scotland sills and isopycnal mixing with intermediate waters further downstream. This
311 mechanisms was already advocated by Dickson et al. (2002) for the preceding 1960s – 1990s cooling and
312 freshening phase, by Sarafanov et al. (2010) for the subsequent warming and salinification phase (1990s –
313 2000s), and most recently to explain the substantial freshening of ISOW in the Iceland Basin (Devana et al.,
314 2021). Such an entrainment-mixing pathway for decadal thermohaline signals is in fact consistent with the
315 recent history of both upper water mass property changes and LSW property changes in the SPNA, which
316 repectively entered a cooling (and freshening) phase circa 2006 and 2012 (Desbruyères et al., 2021; Piron
317 et al., 2017; Robson et al., 2016; Yashayaev & Loder, 2017). This mechanism also concurs with the striking
318 differences in trend magnitudes between ISOW and DSOW. Those differences can be expected from the
319 reported shift in the deep convection pattern towards the Irminger Sea in recent years (Rühs et al., 2021),
320 from the relatively higher dilution of LSW signals between the Labrador Sea and the Iceland-Scotland sills
321 (as compared to the Greenland – Iceland sill), and from isopycnal and diapycnal mixing dilluting ISOW
322 signals before it actually enters the Irminger domain (Petit et al., 2018; Racapé et al., 2019).

324 On top of accounting for a non-negligible fraction of the full water column heat content in the Irminger sea,
325 the temperature trends affecting ISOW and DSOW can have far-reaching impacts on the dynamics of the
326 North Atlantic, including that of its Meridional Overturning Circulation (MOC) whose variability is intimately
327 linked to thermohaline anomalies propagating along the western boundary of the domain (Buckley &
328 Marshall, 2016; Waldman et al., 2020). Specifically, the expected downstream advection within the deep
329 western boundary current of the warming-to-cooling reversal observed herein would in theory imply an
330 intensification of the basin-wide geostrophic shear and hence on the overturning strength. The actual fate
331 of such anomalies as they travel and mix around during their southward journey, including their degree of
332 density-compensation and therefore the influence they can have on a meridionally-coherent mode of MOC
333 variability, remains a motive of current active research.

336 ## Open Research
337 The 1/4° global World Ocean Atlas 2018 (WOA18) was obtained online at
338 https://www.ncei.noaa.gov/data/oceans/woa/WOA18/DATA/. The A25-Ovide sections (2002 – 2018) are
339 available https://doi.org/10.17882/46448. All bottle files (2002 – 2018) are available via the Global Ocean
340 Data Analysis Project (GLODAP) hosted by the Ocean Carbon and Acidification Data System (OCADS) at
341 https://www.ncei.noaa.gov/access/ocean-carbon-acidification-data-
342 system/oceans/RepeatSections/clivar_ovide.html. The Argo data were collected and made freely available
343 by the International Argo Program and the national programs that contribute to it (https://argo.ucsd.edu,
344 https://www.ocean-ops.org/board). The Argo Program is part of the Global Ocean Observing System. The
345 Deep-Argo data used herein are included in the 10th January 2022 snapshot of the Global Data Assembly
346 Centre (Argo GDAC) available via http://doi.org/10.17882/42182#90708. Data for the OSNAP-EI array are
347 available via https://doi.org/10.25850/nioz/7b.b.rb (2014 – 2015), https://doi.org/10.25850/nioz/7b.b.sb
348   (2015-2016),   https://doi.org/10.25850/nioz/7b.b.nb   (2016   –   2018),
349 https://doi.org/10.25850/nioz/7b.b.pb (2018 – 2020).

References

van Aken, H. M., & de Jong, M. F. (2012). Hydrographic variability of Denmark Strait Overflow Water near Cape Farewell with multi-decadal to weekly time scales. *Deep Sea Research Part I: Oceanographic Research Papers*, *66*, 41–50. https://doi.org/https://doi.org/10.1016/j.dsr.2012.04.004

Wong Annie, Robert Keeley, T. C. and the A. D. M. T. (2021). *Argo Quality Control Manual for CTD and Trajectory Data.*

Bindoff, N. L., & Mcdougall, T. J. (1994). Diagnosing Climate Change and Ocean Ventilation Using Hydrographic Data. *Journal of Physical Oceanography*. https://doi.org/10.1175/1520-0485(1994)024<1137:DCCAOV>2.0.CO;2

Le Bras, I. A.-A., Straneo, F., Holte, J., & Holliday, N. P. (2018). Seasonality of Freshwater in the East Greenland Current System From 2014 to 2016. *Journal of Geophysical Research: Oceans*, *123*(12), 8828–8848. https://doi.org/https://doi.org/10.1029/2018JC014511

Broomé, S., Chafik, L., & Nilsson, J. (2020). Mechanisms of decadal changes in sea surface height and heat content in the eastern Nordic Seas. *Ocean Science*, *16*(3), 715–728. https://doi.org/10.5194/os-16-715-2020

Buckley, M. W., & Marshall, J. (2016). Observations, inferences, and mechanisms of the Atlantic Meridional Overturning Circulation: A review. *Reviews of Geophysics*, *54*(1), 5–63. https://doi.org/10.1002/2015RG000493

Daniault, N., Mercier, H., Lherminier, P., Sarafanov, A., Falina, A., Zunino, P., … Gladyshev, S. (2016). The northern North Atlantic Ocean mean circulation in the early 21st century. *Progress in Oceanography*, *146*(June), 142–158. https://doi.org/10.1016/j.pocean.2016.06.007

Desbruyères, D. G., Purkey, S. G., McDonagh, E. L., Johnson, G. C., & King, B. A. (2016). Deep and abyssal ocean warming from 35 years of repeat hydrography. *Geophysical Research Letters*, *43*(19), 10,356-10,365. https://doi.org/10.1002/2016GL070413

Desbruyères, D, McDonagh, E. L., King, B. A., Garry, F. K., Blaker, A. T., Moat, B. I., & Mercier, H. (2014). Full depth temperature trends in the northeastern Atlantic through the early 21st century. *Geophysical Research Letters*, *41*, 7971–7979. https://doi.org/10.1002/2014GL061844.The

Desbruyères, Damien G., Mcdonagh, E. L., King, B. A., & Thierry, V. (2017). Global and Full-Depth Ocean Temperature Trends during the Early Twenty-First Century from Argo and Repeat Hydrography, 1985–1998. https://doi.org/10.1175/JCLI-D-16-0396.1

Desbruyères, D., Chafik, L., & Maze, G. (2021). A shift in the ocean circulation has warmed the subpolar

North Atlantic Ocean since 2016. *Communications Earth & Environment*, *2*(1), 48. https://doi.org/10.1038/s43247-021-00120-y

Devana, M. S., Johns, W. E., Houk, A., & Zou, S. (2021). Rapid Freshening of Iceland Scotland Overflow Water Driven by Entrainment of a Major Upper Ocean Salinity Anomaly. *Geophysical Research Letters*, *48*(22), e2021GL094396. https://doi.org/https://doi.org/10.1029/2021GL094396

Dickson, B., Yashayaev, I., Meincke, J., Turrell, B., Dye, S., & Holfort, J. (2002). Rapid freshening of the deep North Atlantic Ocean over the past four decades. *Nature*, *416*(6883), 832–837. https://doi.org/10.1038/416832a

Foppert, A., Rintoul, S. R., Purkey, S. G., Zilberman, N., Kobayashi, T., Sallée, J., … Wallace, L. O. (2021). Deep Argo reveals bottom water properties and pathways in the Australian-Antarctic Basin. *Journal of Geophysical Research: Oceans*, 1–18. https://doi.org/10.1029/2021jc017935

Fried, N., & de Jong, M. F. (2022). The Role of the Irminger Current in the Irminger Sea Northward Transport Variability. *Journal of Geophysical Research: Oceans*, *127*(3), e2021JC018188. https://doi.org/https://doi.org/10.1029/2021JC018188

Garry, F. K., McDonagh, E. L., Blaker, A. T., Roberts, C. D., Desbruyères, D. G., Frajka-Williams, E., & King, B. A. (2019). Model derived uncertainties in deep ocean temperature trends between 1990-2010. *Journal of Geophysical Research: Oceans*. https://doi.org/10.1029/2018JC014225

Häkkinen, S., Rhines, P. B., & Worthen, D. L. (2015a). Heat content variability in the North Atlantic Ocean in ocean reanalyses. *Geophysical Research Letters*, *42*, 2901–2909. https://doi.org/10.1002/2015GL063299.Received

Häkkinen, S., Rhines, P. B., & Worthen, D. L. (2015b). Heat content variability in the North Atlantic Ocean in ocean reanalyses. *Geophysical Research Letters*, *42*(8), 2901–2909. https://doi.org/https://doi.org/10.1002/2015GL063299

Hansen, B., & Østerhus, S. (2000). North Atlantic–Nordic Seas exchanges. *Progress in Oceanography*, *45*(2), 109–208. https://doi.org/https://doi.org/10.1016/S0079-6611(99)00052-X

Holliday, N. P., Hughes, S. L., Bacon, S., Beszczynska-Möller, A., Hansen, B., Lavín, A., … Walczowski, W. (2008). Reversal of the 1960s to 1990s freshening trend in the northeast North Atlantic and Nordic Seas. *Geophysical Research Letters*, *35*(3), 1–5. https://doi.org/10.1029/2007GL032675

IPCC, Masson-Delmotte, V., Zhai, P., Pirani, A., Connors, S. L., Péan, C., … B., Z. (2021). *Climate Change 2021: The Physical Science Basis. Contribution of Working Group I to the Sixth Assessment Report of the Intergovernmental Panel on Climate Change*. *Cambridge University Press*. Retrieved from https://www.ipcc.ch/report/ar6/wg1/

Johns, W. E., Devana, M., Houk, A., & Zou, S. (2021). Moored Observations of the Iceland-Scotland Overflow Plume Along the Eastern Flank of the Reykjanes Ridge. *Journal of Geophysical Research: Oceans*, *126*(8), e2021JC017524. https://doi.org/https://doi.org/10.1029/2021JC017524

Johnson, G. C. (2019). Deep Argo Quanti fi es Bottom Water Warming Rates in the Southwest Paci fi c Basin Geophysical Research Letters. https://doi.org/10.1029/2018GL081685

Johnson, G. C., Lyman, J. M., & Loeb, N. G. (2016). Improving estimates of Earth's energy imbalance. *Nature Climate Change*, *6*(7), 639–640. https://doi.org/10.1038/nclimate3043

Johnson, G. C., Cadot, C., Lyman, J. M., & Mctaggart, K. E. (2020). Antarctic Bottom Water Warming in the Brazil Basin : 1990s Through 2020 , From WOCE to Deep Argo Geophysical Research Letters. https://doi.org/10.1029/2020GL089191

Johnson, G. C., Lyman, J. M., & Purkey, S. G. (2015). Informing deep argo array design using argo and full-depth hydrographic section data. *Journal of Atmospheric and Oceanic Technology*, *32*(11), 2187–2198. https://doi.org/10.1175/JTECH-D-15-0139.1

Johnson, G. C., Purkey, S. G., Zilberman, N. V, & Roemmich, D. (2019). Deep Argo Quantifies Bottom Water Warming Rates in the Southwest Pacific Basin. *Geophysical Research Letters*, *46*(5), 2662–2669. https://doi.org/10.1029/2018GL081685

453 de Jong, M. F., de Steur, L., Fried, N., Bol, R., & Kritsotalakis, S. (2020). Year-Round Measurements of the
454   Irminger Current: Variability of a Two-Core Current System Observed in 2014–2016. *Journal of*
455   *Geophysical Research: Oceans*, *125*(10), e2020JC016193.
456   https://doi.org/https://doi.org/10.1029/2020JC016193

457 Keeling, R. F., Körtzinger, A., & Gruber, N. (2009). Ocean Deoxygenation in a Warming World. *Annual*
458   *Review of Marine Science*, *2*(1), 199–229. https://doi.org/10.1146/annurev.marine.010908.163855

459 Kobayashi, T. (2018). Rapid volume reduction in Antarctic Bottom Water off the Adélie/George V Land
460   coast observed by deep floats. *Deep-Sea Research Part I: Oceanographic Research Papers*, (July), 1–
461   23. https://doi.org/10.1016/j.dsr.2018.07.014

462 Lherminier, P., Mercier, H., Huck, T., Gourcuff, C., Perez, F. F., Morin, P., … Falina, A. (2010). The Atlantic
463   Meridional Overturning Circulation and the subpolar gyre observed at the A25-OVIDE section in
464   June 2002 and 2004. *Deep-Sea Research Part I: Oceanographic Research Papers*, *57*(11), 1374–1391.
465   https://doi.org/10.1016/j.dsr.2010.07.009

466 Lozier, M. S., Li, F., Bacon, S., Bahr, F., Bower, A. S., Cunningham, S. A., … Zhao, J. (2019). A sea change in
467   our view of overturning in the subpolar North Atlantic. *Science*, *363*(6426), 516 LP – 521.
468   https://doi.org/10.1126/science.aau6592

469 Mercier, H., Lherminier, P., Sarafanov, A., Gaillard, F., Daniault, N., Desbruyères, D., … Thierry, V. (2015).
470   Variability of the meridional overturning circulation at the Greenland-Portugal OVIDE section from
471   1993 to 2010. *Progress in Oceanography*, *132*, 250–261.
472   https://doi.org/10.1016/j.pocean.2013.11.001

473 Petit, T., Mercier, H., & Thierry, V. (2018). First Direct Estimates of Volume and Water Mass Transports
474   Across the Reykjanes Ridge. *Journal of Geophysical Research: Oceans*, (Figure 2), 6703–6719.
475   https://doi.org/10.1029/2018JC013999

476 Piron, A., Thierry, V., Mercier, H., & Caniaux, G. (2017). Gyre-scale deep convection in the subpolar North
477   Atlantic Ocean during winter 2014???2015. *Geophysical Research Letters*, *44*(3), 1439–1447.
478   https://doi.org/10.1002/2016GL071895

479 Purkey, S. G., & Johnson, G. C. (2010). Warming of global abyssal and deep Southern Ocean waters
480   between the 1990s and 2000s: Contributions to global heat and sea level rise budgets. *Journal of*
481   *Climate*, *23*(23), 6336–6351. https://doi.org/10.1175/2010JCLI3682.1

482 Racapé, V., Thierry, V., Mercier, H., & Cabanes, C. (2019). ISOW spreading and mixing as revealed by
483   Deep-Argo floats launched in the Charlie Gibbs Fracture Zone. *Journal of Geophysical Research:*
484   *Oceans*, *0*(ja). https://doi.org/10.1029/2019JC015040

485 Riser, S. C., Freeland, H. J., Roemmich, D., Wijffels, S., Troisi, A., Belbéoch, M., … Jayne, S. R. (2016).
486   Fifteen years of ocean observations with the global Argo array. *Nature Climate Change*, *6*(2), 145–
487   153. https://doi.org/10.1038/nclimate2872

488 Robson, J., Ortega, P., & Sutton, R. (2016). A reversal of climatic trends in the North Atlantic since 2005.
489   *Nature Geoscience*, *9*(7), 513–517. https://doi.org/10.1038/ngeo2727

490 Roemmich, D., Alford, M. H., Claustre, H., Johnson, K. S., King, B., Moum, J., … Yasuda, I. (2019). On the
491   future of Argo: A global, full-depth, multi-disciplinary array. *Frontiers in Marine Science*.
492   https://doi.org/10.3389/fmars.2019.00439

493 Rühs, S., Oliver, E. C. J., Biastoch, A., Böning, C. W., Dowd, M., Getzlaff, K., … Myers, P. G. (2021). Changing
494   Spatial Patterns of Deep Convection in the Subpolar North Atlantic. *Journal of Geophysical Research:*
495   *Oceans*, *126*(7), e2021JC017245. https://doi.org/https://doi.org/10.1029/2021JC017245

496 Sallée, J.-B., Pellichero, V., Akhoudas, C., Pauthenet, E., Vignes, L., Schmidtko, S., … Kuusela, M. (2021).
497   Summertime increases in upper-ocean stratification and mixed-layer depth. *Nature*, *591*(7851),
498   592–598. https://doi.org/10.1038/s41586-021-03303-x

499 Sarafanov, A., Sokov, A., Demidov, A., & Falina, A. (2007). Warming and salinification of intermediate and
500   deep waters in the Irminger Sea and Iceland Basin in 1997–2006. *Geophysical Research Letters*,

501   *34*(23). https://doi.org/https://doi.org/10.1029/2007GL031074

502 Sarafanov, A., Mercier, H., Falina, A., Sokov, E., & Lherminier, P. (2010). Cessation and partial reversal of
503   deep water freshening in the northern North Atlantic: observation-based estimates and attribution.
504   *Tellus A*, *62*(1), 80–90. https://doi.org/https://doi.org/10.1111/j.1600-0870.2009.00418.x

505 Von Schuckmann, K., Cheng, L., Palmer, M. D., Hansen, J., Tassone, C., Aich, V., … Wijffels, S. E. (2020).
506   Heat stored in the Earth system: Where does the energy go? *Earth System Science Data*, *12*(3),
507   2013–2041. https://doi.org/10.5194/essd-12-2013-2020

508 Talley, L. D., Pickard, G. L., Emery, W. J., & Swift, J. H. (2011). Chapter 9 - Atlantic Ocean. In L. D. Talley, G.
509   L. Pickard, W. J. Emery, & J. H. B. T.-D. P. O. (Sixth E. Swift (Eds.), *Descriptive Physical Oceanography*
510   *(Sixth Edition). An Introduction.* (pp. 245–301). Boston: Academic Press.
511   https://doi.org/https://doi.org/10.1016/B978-0-7506-4552-2.10009-5

512 Tebaldi, C., Ranasinghe, R., Vousdoukas, M., Rasmussen, D. J., Vega-Westhoff, B., Kirezci, E., … Mentaschi,
513   L. (2021). Extreme sea levels at different global warming levels. *Nature Climate Change*, *11*(9), 746–
514   751. https://doi.org/10.1038/s41558-021-01127-1

515 Waldman, R., Hirschi, J., Voldoire, A., Cassou, C., & Msadek, R. (2020). Clarifying the relation between
516   AMOC and thermal wind: application to the centennial variability in a coupled climate model.
517   *Journal of Physical Oceanography*, 1–61. https://doi.org/10.1175/jpo-d-19-0284.1

518 Yashayaev, I., Holliday, N. P., Bersch, M., & van Aken, H. M. (2008). The History of the Labrador Sea
519   Water: Production, Spreading, Transformation and Loss. In R. R. Dickson, J. Meincke, & P. Rhines
520   (Eds.), *Arctic--Subarctic Ocean Fluxes: Defining the Role of the Northern Seas in Climate* (pp. 569–
521   612). Dordrecht: Springer Netherlands. https://doi.org/10.1007/978-1-4020-6774-7_25

522 Yashayaev, I., & Loder, J. W. (2016). Recurrent replenishment of Labrador Sea Water and associated
523   decadal-scale variability. *Journal of Geophysical Research: Oceans*, *121*(11), 8095–8114.
524   https://doi.org/10.1002/2016JC012046

525 Yashayaev, I., & Loder, J. W. (2017). Further intensification of deep convection in the Labrador Sea in
526   2016. *Geophysical Research Letters*, *44*(3), 1429–1438. https://doi.org/10.1002/2016GL071668

527 Zilberman, N. V, Roemmich, D. H., & Gilson, J. (2020). Deep-Ocean Circulation in the Southwest Pacific
528   Ocean Interior: Estimates of the Mean Flow and Variability Using Deep Argo Data. *Geophysical*
529   *Research Letters*, *47*(13), e2020GL088342. https://doi.org/https://doi.org/10.1029/2020GL088342

530

531